

# UC San Diego

## UC San Diego Previously Published Works

### Title

High-pressure nano-seismology: Use of micro-ring resonators for characterizing acoustic emissions

### Permalink

<https://escholarship.org/uc/item/4x4794q2>

### Journal

Applied Physics Letters, 115(8)

### ISSN

0003-6951 1077-3118

### Authors

Smart, T.  
Li, H.  
Dong, B.  
[et al.](#)

### Publication Date

2019-08-19

### DOI


10.1063/1.5113496

Peer reviewed

# High-pressure nano-seismology: Use of micro-ring resonators for characterizing acoustic emissions

Cite as: Appl. Phys. Lett. **115**, 081904 (2019); <https://doi.org/10.1063/1.5113496>

Submitted: 10 June 2019 . Accepted: 03 August 2019 . Published Online: 22 August 2019

T. Smart , H. Li, B. Dong, X. Shu, R. Hai, C. Sun, H. F. Zhang, and R. Jeanloz



View Online



Export Citation



CrossMark

## ARTICLES YOU MAY BE INTERESTED IN

[Experimental validation of deep-subwavelength diffusion by acoustic metadiffusers](#)

Applied Physics Letters **115**, 081901 (2019); <https://doi.org/10.1063/1.5114877>

[Hydrogel-mediated semiconductor wafer bonding](#)

Applied Physics Letters **115**, 081601 (2019); <https://doi.org/10.1063/1.5096540>

[Focused acoustic vortex by an artificial structure with two sets of discrete Archimedean spiral slits](#)

Applied Physics Letters **115**, 083501 (2019); <https://doi.org/10.1063/1.5108687>

Lock-in Amplifiers  
up to 600 MHz



Watch



# High-pressure nano-seismology: Use of micro-ring resonators for characterizing acoustic emissions

Cite as: Appl. Phys. Lett. **115**, 081904 (2019); doi: [10.1063/1.5113496](https://doi.org/10.1063/1.5113496)

Submitted: 10 June 2019 · Accepted: 3 August 2019 ·

Published Online: 22 August 2019



View Online



Export Citation



CrossMark

T. Smart,<sup>1,a)</sup>  H. Li,<sup>2</sup> B. Dong,<sup>2,3</sup> X. Shu,<sup>2</sup> R. Hai,<sup>3</sup> C. Sun,<sup>3</sup> H. F. Zhang,<sup>2</sup> and R. Jeanloz<sup>1</sup>

## AFFILIATIONS

<sup>1</sup>Department of Earth and Planetary Science, University of California in Berkeley, Berkeley, California, 94720, USA

<sup>2</sup>Department of Biomedical Engineering, Northwestern University, Evanston, Illinois, 60208, USA

<sup>3</sup>Department of Mechanical Engineering, Northwestern University, Evanston, Illinois, 60208, USA

<sup>a)</sup>Electronic mail: [Tsmart@berkeley.edu](mailto:Tsmart@berkeley.edu)

## ABSTRACT

Microring resonator (MRR) ultrasound detectors provide orders of magnitude greater sensitivity and frequency range (to  $< 10$  Pa, from DC to 100 s of MHz) than previously achieved in recording acoustic emissions from materials at high pressures. We characterize acoustic emissions from crystal-structural phase transitions in Si to pressures of 50 GPa, well beyond the brittle-ductile transition at room temperature, and find that the number of events increases nearly tenfold for each decade reduction in the duration of recorded events. The shortest-duration events arrive in clusters, suggestive of a self-propagating, transformation-catalyzed process.

Published under license by AIP Publishing. <https://doi.org/10.1063/1.5113496>

Acoustic emissions present a fundamental conundrum in the deformation behavior of materials at pressures exceeding 1–3 GPa, because yielding is by ductile flow rather than brittle fracture at these pressures.<sup>1</sup> This is due to the normal forces across incipient shear planes being sufficiently large to prevent fracture in the material. Still, emissions have been documented in connection with phase transformations at pressures well above the brittle-ductile transition,<sup>2–6</sup> using detectors sensitive to frequencies of 2–20 MHz. Given that the time for an acoustic wave to traverse the samples in these studies is on the order of  $10^{-7}$  s,<sup>2</sup> and is comparable to the sampling rate, past work has been limited in its ability to resolve fine detail in the acoustic emissions of materials at high pressures.

Here, we describe an optoelectronic method for characterizing acoustic emissions from samples at high pressure, the objective being to increase sensitivity and frequency range relative to past capabilities.<sup>7,8</sup> Briefly, the microring resonator uses tunneling of light (evanescent waves) between a through-going optical bus waveguide and whispering gallery modes (WGMs) in a neighboring ring waveguide (Fig. 1). The underlying optical resonance provides high sensitivity to transient-pressure induced modulation of the resonance mode, down to less than 10 Pa as compared with 1–55 kPa typical of commercial piezoelectric sensors.<sup>9</sup> Sensitivity is also enhanced by using a soft (compliant) polymeric material, in our case, polystyrene.

Because light modulation carries the signal, the sensor is, in principle, responsive to frequencies into the terahertz range. As described below, however, our current system is effective only up to frequencies

of  $\sim 250$  MHz: still, 1–2 orders of magnitude higher than for previous high-pressure measurements.<sup>3,5,6</sup> For a shear-wave velocity of 5 km/s, this implies sensitivity to acoustic wavelengths down to  $\sim 20$   $\mu\text{m}$ , comparable to our sample dimensions and approaching the size of grains, if not the stress field at shear- and tensile-fracture tips for Si at ambient conditions (the process zone of ductile deformation at the fracture tip is yet smaller,  $\sim 2$ –5 nm).<sup>10–14</sup>

Silicon powder (grain size of  $\sim 10$   $\mu\text{m}$ ) was compressed in Merrill-Basset type diamond-anvil cells without any pressure medium, as our intent was to generate shear stresses under high pressure. The diamonds had culet diameters of 350  $\mu\text{m}$ , paired with a 250  $\mu\text{m}$ -thick spring-steel gasket pre-compressed to 70–90  $\mu\text{m}$  thickness and containing a 150  $\mu\text{m}$ -diameter hole as the sample chamber. A film of ruby powder  $\sim 5$   $\mu\text{m}$  thick ( $\sim 1$   $\mu\text{m}$  grain size) was added to the culet of one of the diamonds for pressure calibration, using ruby fluorescence.<sup>15</sup>

As described by Li and Dong *et al.*<sup>7</sup> the microring resonator (MRR) ultrasound detector is placed on a 2 mm  $\times$  2 mm fused silica coverslip. The polystyrene optical waveguide has a square-shaped cross section, 800 nm across, and both the input and output ends of this bus waveguide are precisely cleaved for fiber coupling. To excite optical resonance in the MRR, a narrow-band continuous-wave (CW) tunable laser (New Focus, TLB-6712, wavelength 765 nm–781 nm) is coupled into the bus waveguide after passing through a fiber polarization controller. On the other end of the bus waveguide, a multimode fiber and photodetector (Newport, 2107-FC) are used to measure the transmitted light intensity.

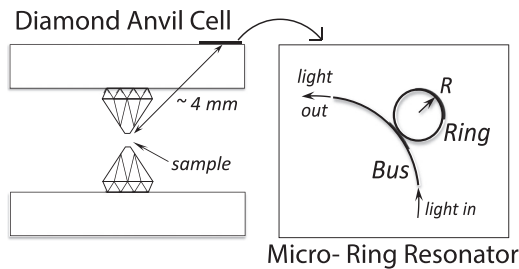


**FIG. 1.** Schematic of microring resonator and diamond-anvil cell used in the present experiments (not to scale). Light transmitted down the bus fiber is evanescently coupled into the ring (radius  $R \sim 30 \mu\text{m}$ ) such that an acoustic wave temporarily modulates the light exiting the bus. The polystyrene fiber optics are placed on a  $2 \times 2 \text{ mm}$  silica glass slide, which is attached to the body of the diamond cell. The location of the sample is between the diamond tips (culets), and for clarity, no gasket is shown.

The light inside the bus waveguide is evanescently coupled into the ring waveguide across a low-dielectric gap between the bus and the ring. Light circulating inside the ring waveguide leads to a strong optical resonance to be characterized by a narrow dip in the transmission spectrum due to destructive interference between light in the two waveguides. Minimum transmission is achieved at the resonance wavelength ( $\lambda_r$ ) at critical coupling, when the intrinsic loss of the ring resonator matches the coupling loss. The quality ( $Q$ ) factor of the MRR is determined from the measured transmission spectrum,  $T(\lambda)$ , as  $\lambda_r/\Delta\lambda = 1.2 \times 10^5$ , where  $\Delta\lambda$  is the full width at half-maximum of the resonance dip. The MRR operating wavelength is set slightly off resonance, at the waist of the resonance dip, to achieve an optimal detection sensitivity of  $dT/d\lambda = 30.24 \text{ nm}^{-1}$  at  $776.25 \text{ nm}$ .

Acoustic waves induce changes in both the dimension and refractive index of the polymer ring, collectively altering the optical path length of the ring resonator, thus shifting the resonant frequency. The shift in resonant frequency is measured as a voltage modulation in the transmitted optical signal by a photodetector. We used a low-noise, high-sensitivity avalanche photodiode (APD, Hamamatsu c4777) to record the transmitted light through the bus waveguide. The detected signals were then amplified by 12 dB (Mini-circuits ZFL500NL+, 500-MHz bandwidth) and digitized by a high-speed digitizer (CobraMax, GaGe; sampling rate:  $3 \times 10^9$  samples/s, bandwidth: 1.5 GHz). This sensor provides a broad detection band of over 100 MHz and a pressure detection limit of 6.8 Pa.

The MRR assembly was mounted on the steel body of the diamond-anvil cell (Fig. 1), which was held in a clamp mounted to an air-floating optical table, and elevated above the surface of the table to reduce ambient noise. Samples were compressed at room temperature up to pressures of 50 GPa, and acoustic emissions were monitored during both compression and decompression cycles. The MRR detector was about 4 mm away from the polycrystalline silicon sample and was set to trigger during and after the pressure changes were being applied. All measurements were made at  $19\text{--}22^\circ\text{C}$ .

A series of control experiments were conducted to pressures exceeding 35 GPa, using both steel and rhenium gaskets. Inside the sample chamber, we loaded (i) no pressure medium (in order to record any acoustic emissions from the empty sample chamber closing); (ii) a neon pressure medium; or (iii) a 4:1 methanol:ethanol

**TABLE I.** Phase transitions and corresponding pressure ranges during which we observe an acoustic emission in Si at room temperature. All transitions associated with acoustic emissions yielded acoustic events on the order of  $10^{-7}$  s, though the maximum duration appears to vary between different phase transitions. The maximum duration of recorded acoustic events is shown.

	Phase transition	Pressure range (GPa)	Maximum emission duration (s)
Compression	Si-I $\rightarrow$ Si-II	11–12	$10^{-7}$
	Si-II $\rightarrow$ Si-XI	13–15	No Emission
	Si-XI $\rightarrow$ Si-V	16–17	$10^{-3}$
Decompression	Si-V $\rightarrow$ Si-III	9–11	$10^{-4}$
Recompression	Si-III $\rightarrow$ Si-V	13–17	$10^{-5}$

pressure medium. We also ran tests on plain metal foils (i.e., gaskets with no sample chamber) to further test the gasket material for acoustic emission. None of these control experiments yielded any acoustic emissions, indicating that the signals we report over this pressure range are caused by the deformation of the silicon sample.

We recorded acoustic emissions in silicon to 17 GPa on compression and decompression, well above the brittle-ductile transition, estimated around 1.5 GPa at room temperature,<sup>14</sup> as confirmed by observing the sample to flow in a ductile manner during compression. During the initial compression, acoustic emissions were measured at the Si-I (diamond structure)  $\rightarrow$  Si-II ( $\beta$ -Sn structure) transformation between 11 and 12 GPa. On further compression, emissions were recorded acoustic signals between 16 and 17 GPa, corresponding to the Si-XI (orthorhombic, *Imma*)  $\rightarrow$  Si-V (simple hexagonal) transition. Signals were also recorded on decompression from the high-pressure Si phases to the metastable Si-III (bcc) phase around 11 GPa (see Table I).<sup>2,16–19</sup> Cycling the sample by decompression and recompression into low- and high-pressure phases consistently yielded acoustic emissions at these conditions. In contrast, we recorded no acoustic emissions while crossing the Si-II  $\rightarrow$  XI, V  $\rightarrow$  VI, and VI  $\rightarrow$  VII phase transitions at  $\sim 15$ ,  $\sim 34$ , and  $\sim 40$  GPa, respectively, either during compression or decompression. Evidently, not all phase transitions produce acoustic emissions, at least over the frequency range and within the sensitivity of our detection system (this point is also relevant to the lack of acoustic emissions from any of our present gasket materials).

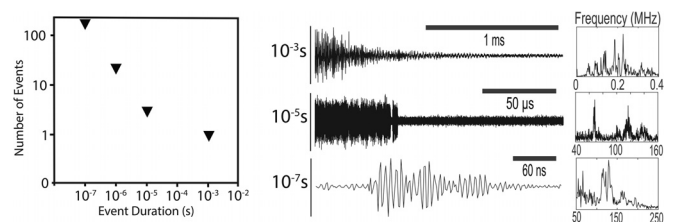


**FIG. 2.** Acoustic signals collected from Si between 14 and 17 GPa, showing that the number of events decreases with increased event duration (“left”). Signals with durations of  $10^{-5}$  s and  $10^{-7}$  s (“middle”) have strong peaks around 120 MHz in their power spectra (“right”), corresponding to wavelengths comparable to or smaller than the thickness of our sample chamber. Signals approaching millisecond duration exhibit a significantly different power spectrum, with no signal recorded above 0.5 MHz, suggesting either a change in failure mechanism or that the amplitude of the low-frequency emission obscures higher-frequency signals.

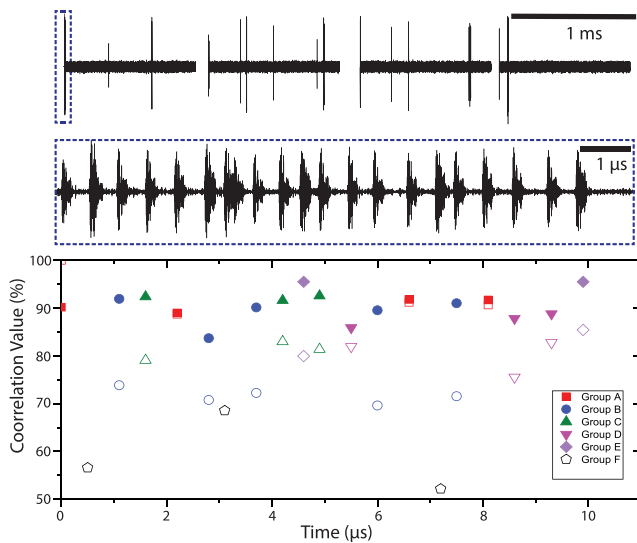


**FIG. 3.** A  $\sim 5$  ms record is shown (“top”), displaying acoustic-emission bursts at apparently random intervals. Each burst at the millisecond time scale is found to consist of several roughly periodic emissions (“middle.”) Cross-correlation (“bottom”) shows 50–90% correspondence between the first signal ( $0 < t < 0.4 \mu\text{s}$ ) and subsequent emissions (“open symbols,” plotted directly below each given emission). Groups, identified as signals having similar correlation values relative to the primary emission, are also found to produce significantly higher (85–95%) correlations when compared with one another (“filled, color symbols”: none for Group F), suggesting similarities in source mechanisms for signals in a group.

The duration of individual acoustic events from our samples ranges from  $10^{-7}$  s to  $10^{-3}$  s, roughly following a power law with the number of emissions, decreasing by nearly one order of magnitude for each decade increase in duration (exponent  $\sim 0.8$ – $1.0$ ) (Fig. 2, “left panel”). For a given rupture, the event duration is proportional to the seismic moment and magnitude, allowing us to compare this result with moment-magnitude distributions observed in seismology (e.g., Gutenberg–Richter law). Our results closely follow observations made in past laboratory and field observations of rupturing, including acoustic emissions from high-pressure multianvil experiments.

Samples that produce only short emissions on compression often yield additional signals upon further compression, but this was not the case for samples emitting signals longer than  $\sim 10^{-5}$  s. Emissions with durations on the order of 1 ms were audible at a distance of  $\sim 1$  m, and the resulting deformation of the sample was visible under the microscope, with displacements exceeding 1–10  $\mu\text{m}$ . Acoustic emissions shorter than  $10^{-3}$  s were not audible and showed no visible sample deformation.

Short ( $\sim 200$  ns) emissions are observed for all of the acoustically active phase transitions, both on their own and as part of longer events. Comparison of these short emissions between sample runs shows a consistent structure of three pulses, each about 60 ns long (Fig. 2, “bottom of the middle panel”), and with peak frequencies of 120–140 MHz. Acoustic events longer than  $10^{-7}$  s displayed peak frequencies identical to those of the shortest emissions, as well as at lower frequencies as would be expected. These longer events consist of a high density of short emissions, as also indicated by the  $>100$  MHz peaks in the power spectra (Fig. 2, “middle of the right panel”).

When short-duration ( $\sim 200$  ns) signals are not part of a longer signal, there is a tendency for the emissions to cluster into groups of 5–20 events. These clusters do not show the high correlations and decaying amplitudes one would expect from successive echoes and so are interpreted as individual nanoseismic events (Fig. 3). Short-duration emissions show cross-correlations ranging between 70 and 90%. Also, emissions with a similar correlation value to a given signal (e.g., the initial burst) show high (85–95%) mutual correlations (closed symbols in Fig. 3), suggesting that the emissions within that group are related (Fig. 3). These mutually correlated emissions may have sources that are similar in orientation or other characteristics. Note that a 100 ns signal implies a rupture propagating across the full diameter of our sample (150  $\mu\text{m}$ ) for a rupture velocity less than  $1/3$  the shear-wave velocity ( $V_S$  is 5 km/s or 5  $\mu\text{m}/\text{ns}$  at zero pressure).

The temporal spacing between acoustic clusters appears random (Fig. 3, “top panel”). When subjected to a test of randomness, the intervals are found to follow a Poisson distribution with an average of 0.24 events per  $\mu\text{s}$ , implying that the clusters are independent of each other. However, the temporal spacing is more regular within a given cluster (Fig. 3, “middle panel”), suggesting a catalytic process in which one acoustic emission triggers subsequent events in the cluster.

We would like to thank Professors Steve Jacobsen and Douglas Dreger, as well as Michelle Wenz, Nate Lindsay, and Sierra Boyd, for helpful discussions. We additionally thank Professor Jacobsen for the use of his Raman spectrometer. This work was supported by the University of California, the United States National Nuclear Security Administration and Department of Energy, and the National Science Foundation fund No. NSF DBI-135395.

## REFERENCES

- <sup>1</sup>M. S. Paterson and T.-F. Wong, *Experimental Rock Deformation—The Brittle Field*, 2nd ed. (Springer, New York, 2005), pp 211–237.
- <sup>2</sup>C. Meade and R. Jeanloz, *Nature* **339**(6226), 616 (1989).
- <sup>3</sup>C. Meade and R. Jeanloz, *Science* **252**(5002), 68 (1991).
- <sup>4</sup>A. A. de Ronde and D. P. Dobson, *High Pressure Res.* **28**(1), 9 (2008).
- <sup>5</sup>A. Schubnel, F. Brunet, N. Hilaret, J. Gasc, Y. B. Wang, and H. W. Green, *Science* **341**(6152), 1377 (2013).
- <sup>6</sup>H. M. Wei and S. Krishnaswamy, *Opt. Lett.* **42**(13), 2655 (2017).
- <sup>7</sup>H. Li, B. Q. Dong, Z. Zhang, H. F. Zhang, and C. Sun, *Sci. Rep.* **4**, 8 (2014).
- <sup>8</sup>H. Wei, A. K. Amrithanath, and S. Krishnaswamy, *Proc. SPIE* **10600**, 1060003 (2018).
- <sup>9</sup>B. Q. Dong, C. Sun, and H. F. Zhang, *IEEE Trans. Biomed. Eng.* **64**(1), 4 (2017).
- <sup>10</sup>A. G. Haerle, W. R. Cannon, and M. Denda, *J. Am. Ceram. Soc.* **74**(11), 2897 (1991).
- <sup>11</sup>I. Chasiotis, S. W. Cho, and K. Jonnalagadda, *J. Appl. Mech.-Trans. ASME* **73**(5), 714 (2006).
- <sup>12</sup>R. F. Cook, *J. Mater. Sci.* **41**(3), 841 (2006).
- <sup>13</sup>B. N. Jaya, J. M. Wheeler, J. Wehrs, J. P. Best, R. Soler, J. Michler, C. Kirchlechner, and G. Dehm, *Nano Lett.* **16**(12), 7597 (2016).
- <sup>14</sup>H. J. Frost and M. F. Ashby, *Deformation Mechanism Maps* (Pergamon, Oxford, UK, 1982), pp.71–74.
- <sup>15</sup>H. K. Mao, J. Xu, and P. M. Bell, *J. Geophys. Res., Solid Earth Planets* **91**(B5), 4673, <https://doi.org/10.1029/JB091iB05p04673> (1986).
- <sup>16</sup>J. Z. Hu and I. L. Spain, *Solid State Commun.* **51**(5), 263 (1984).
- <sup>17</sup>H. Olijnyk, S. K. Sikka, and W. B. Holzapfel, *Phys. Lett. A* **103**(3), 137 (1984).
- <sup>18</sup>M. I. McMahon, R. J. Nelmes, N. G. Wright, and D. R. Allan, *Phys. Rev. B* **50**, 739 (1994).
- <sup>19</sup>A. Kubo, Y. Wang, C. Runge, T. Uchida, B. Kiefer, N. Nishiyama, and T. Duffy, *J. Phys. Chem. Solids* **69**(9), 2255 (2008).